









Sm/Al modified $\text{Sn}_{0.94}\text{Sb}_{0.06}\text{O}_2$ ceramics for NTC thermistors

You Zhang ¹, Hong Zhang ¹, Hao Chen ¹, Yifei Zhan ¹, Zhicheng Li ^{1,*},
Senlin Leng ^{2,*}

¹School of Materials Science and Engineering, Central South University, Changsha 410083, China

²School of Material and Chemical Engineering, Tongren University, Tongren 554300, China

Received 5 April 2024; Received in revised form 18 May 2024; Accepted 30 May 2024

Abstract

Negative temperature coefficient (NTC) thermistors are key components for temperature sensors and actuators. In this work, $\text{Sn}_{0.94-x-y}\text{Al}_x\text{Sm}_y\text{Sb}_{0.06}\text{O}_{2+\delta}$ ($0 \leq x \leq 0.05$, $0 \leq y \leq 0.15$) ceramics were prepared by solid-state reaction method for potential application of NTC thermistors. The Sm/Al co-doped SnO_2 ceramics had the main phase with tetragonal structure as that of SnO_2 crystal. The prepared ceramics presented adjustable room temperature resistivity (ρ_{25}) and temperature sensitivity (B value) for various Al contents. Sm/Al co-doping significantly improved the ageing stability, the resistance shift rate was below 3% after ageing at 150 °C for 500 h, while the average resistance shift rate was 41.4% of the ceramics without Sm-doping. The conduction mechanisms and the effect of dopants on the ageing stability were investigated by analysis of impedance spectra and element valences combined with defect chemistry theory.

Keywords: SnO_2 , element doping, thermistors, NTC, electrical property

I. Introduction

Negative temperature coefficient (NTC) thermistors are the key components of temperature sensing elements and have attracted much attention due to their high temperature sensitivity, rapid responsiveness, low cost, etc. [1]. The NTC thermistors have been widely applied in temperature sensing, temperature measurement, temperature compensation and circuit protection [2–4]. Based on the chemical composition of the main phase, the normal-temperature type NTC thermistors can be generally divided into two systems: multi-component compounds and single cation oxides. The former system consist of spinel type compounds such as manganates or perovskite type compounds [5–11]. The NTC thermistors based on the single cation oxides (SCOs) such as ZnO, CuO, NiO and SnO_2 have been intensely studied in recent years [12–21]. The SCO NTC thermistors have their unique characteristics, i.e. room-temperature resistivity (ρ_{25}) and temperature sensitivity (B value), which can be effectively regulated by element doping and solid solution treatment. Yang *et al.* [17] reported that NiO based ceramics showed typical NTC features with ad-

justable B values ranging from 2582 to 6043 K and ρ_{25} ranging from 0.08 to 10.68 k Ω -cm by being doped by various contents of B^{3+} and Na^+ cations. Yang *et al.* [20] received CuO based NTC ceramics with B values ranging from 1112 to 3700 K and ρ_{25} ranging from 80 to 2.75 M Ω -cm when the ceramics were modified with various concentrations of Ti^{4+} and Y^{3+} cations. The significance of achieving adjustable B value and ρ_{25} is to make products suitable for various application requirements.

As a typical SCO semiconductor, SnO_2 has been extensively studied in the field of gas sensors [22], dielectrics [23], varistors [24], etc. As previously reported, the SnO_2 based ceramics doped with Sb-ions (antimony tin oxide, abbreviated as ATO) can get low ρ_{25} [25,26], and the optimized doping contents of Sb-ions are between 4 and 7 mol%. However, the related B values of ATO ceramics are too small (lower than 400 K) to meet the application requirement (2000–5000 K [1]). In present work, in order to develop a new ATO-based NTC ceramics, ATO ceramics doped with Sm^{3+} ions, Al^{3+} ions and $\text{Sm}^{3+}/\text{Al}^{3+}$ ions were fabricated. The results show that the doped ATO ceramics presented adjustable B and ρ_{25} values for various contents of dopants, and the Sm/Al co-doping can effectively enhance the ageing stability of ATO-based NTC ceram-

*Corresponding author: tel: +86 13975895660
e-mail: zhchli@csu.edu.cn (Zhicheng Li)
764546880@qq.com (Senlin Leng)

ics. The analyses of phase components, microstructure and ions valence state were conducted to investigate the electrical properties of the fabricated ceramics.

II. Experimental

2.1. Material preparation

A series of ceramics with nominal formula of $\text{Sn}_{0.94-x-y}\text{Al}_x\text{Sm}_y\text{Sb}_{0.06}\text{O}_{2+\delta}$ ($0 \leq x \leq 0.05$, $0 \leq y \leq 0.15$) were prepared by a solid-state reaction method. Here, $\text{Sn}_{0.94}\text{Sb}_{0.06}\text{O}_2$ is denoted as ATO, the samples of Al-doped ATO ($\text{Sn}_{0.94-x}\text{Al}_x\text{Sb}_{0.06}\text{O}_{2+\delta}$) without Sm-ion are denoted as $x\text{Al-ATO}$, the ones of Sm-doped ATO ($\text{Sn}_{0.94-y}\text{Sm}_y\text{Sb}_{0.06}\text{O}_{2+\delta}$) without Al-ion are denoted as $y\text{Sm-ATO}$, and Al/Sm co-doped ATO samples ($\text{Sn}_{0.91-z}\text{Al}_z\text{Sm}_{0.03}\text{Sb}_{0.06}\text{O}_{2+\delta}$) are denoted as $z\text{SA-ATO}$. The raw materials were tin oxide (SnO_2 , Xilong chemical Co. Ltd, China), antimony oxide (Sb_2O_3 , Xilong chemical Co. Ltd, China), aluminium hydroxide ($\text{Al}(\text{OH})_3$, Hunan Xiangzhong, China) and samarium oxide (Sm_2O_3 , Baotou rare earth new materials Co. Ltd, China). The appropriate amounts of raw materials were weighed according to the nominal formula for each batch and were mixed by ball milling for 4 h with deionized water, then dried in an oven at 120°C for 12 h. The dried mixtures were calcined at 950°C for 5 h in air. After that, 2 wt.% CuO (99%, Shanghai Macklin Biochemical Co. Ltd, China) was added into the calcined powder to improve sinterability. The calcined powders were granulated with moderate polyvinyl alcohol (PVA) and then pressed into disc pellets with a diameter of 12 mm and a thickness of about 2 mm under a uniaxial static pressure of 10 MPa. The green pellets were sintered at 1350°C for 2 h in air. To implement electrical properties measurements, the opposite surfaces of the sintered ceramics were polished and coated with silver paste, and then treated at 600°C for 2 min to get ohmic electrodes.

For ageing test, the samples were put into an oven at 150°C in air for 500 h. All samples were pre-processed for 50 h in oven to obtain effective measurement results. During the ageing process, the samples were taken out from the oven after being heated for about every 50 h and put at room temperature for at least 1 h before resistance measurement.

2.2. Characterization

The phase composition and lattice parameters of the sintered ceramics were characterized by X-ray diffractometer (XRD, Rigaku D/max 2500, Japan) with Cu K_α radiation with wavelength of 0.154056 nm. The microstructure of ceramics was observed through a scanning electron microscope (SEM, JMS-7900 F). The element distribution characterization was conducted by an energy dispersive X-ray spectroscopy (EDS, Oxford Ultim Max 65) attached to the SEM. Chemical valence analysis was performed by X-ray photoelectron spectroscopy (XPS, K-alpha 1063, UK). Two tests were performed on the same sample, before and after age-

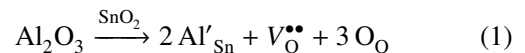
ing. The densities of all ceramics were obtained by the Archimedes method in water.

A resistance-temperature (R - T) measurement system (ZWX-C, Huazhong University of Science and Technology, China) was used to measure the resistances over temperature range between 25 and 200°C , at direct current (DC) condition. Moreover, an alternating current (AC) impedance measurement was carried out by an electrochemical workstation (Gamry Reference 600, USA), in frequency range from 1 Hz to 1 MHz.

III. Results and discussion

3.1. Phase and microstructure

XRD patterns of the prepared ATO-based ceramics are presented in Fig. 1. Figure 1a confirms that the pure ATO ceramics has a single phase tetragonal SnO_2 structure with space group of $P42/mnm$ (136) (referred by PDF No. 01-075-2893). On the other hand, all Sm/Al co-doped samples ($z\text{SA-ATO}$) consist of a main tetragonal SnO_2 phase and a trace of cubic Sm_2O_3 type phase with a space group of $Fm\bar{3}m$ (225) (referred by PDF No. 01-071-6404). Partially magnified view of XRD patterns around the peak from (110) plane is shown in Fig. 1b. With the increase of Al-ions content to $x = 0.027$, the XRD peak shifted toward higher diffraction angles. This indicates that the lattice parameters decreased as the content of Al-ions increased. However, when the content of Al-ions increased to $x = 0.03$ in the $z\text{SA-ATO}$, the XRD peak shifted toward lower diffraction angle, implying that the lattice parameter decreased. Refined by Jade 6.0 + pdf2004 program, the detailed lattice parameters and lattice density of the $z\text{SA-ATO}$ samples are listed in Table 1. The lattice parameters of the samples decreased while the Al content increased up to $x \leq 0.027$. The substitution of smaller Al^{3+} ions into Sn^{4+} sites led to the reduction of $[\text{SnO}_6]$ octahedrons and the occurrence of oxygen vacancies, resulting in a decrease of lattice size. The related defect chemical reaction can be presented in Eq. 1:



The lattice parameter of the 0.03SA-ATO became larger than that of the 0.027SA-ATO ceramics, indicating that some Al-ions occupied interstitial sites [27].

XRD pattern of the 0.03Sm-ATO ceramics without Al-dopant is composed of main SnO_2 phase and impurity Sm_2O_3 phase (Fig. 1c), while the 0.03Al-ATO ceramics without Sm-ion has a single phase tetragonal SnO_2 structure (Fig. 1d). These imply that the solid solubility of Al^{3+} ions in SnO_2 crystal is large enough while the solid solubility of Sm^{3+} ions in SnO_2 is limited. The discrepancy of solubility should be due to the different ionic radii (1.079 \AA for Sm^{3+} , 0.53 \AA for Al^{3+} and 0.69 \AA for Sn^{4+} in 6-fold coordination state [28]). The slightly smaller Al-ions entered SnO_2 lattice

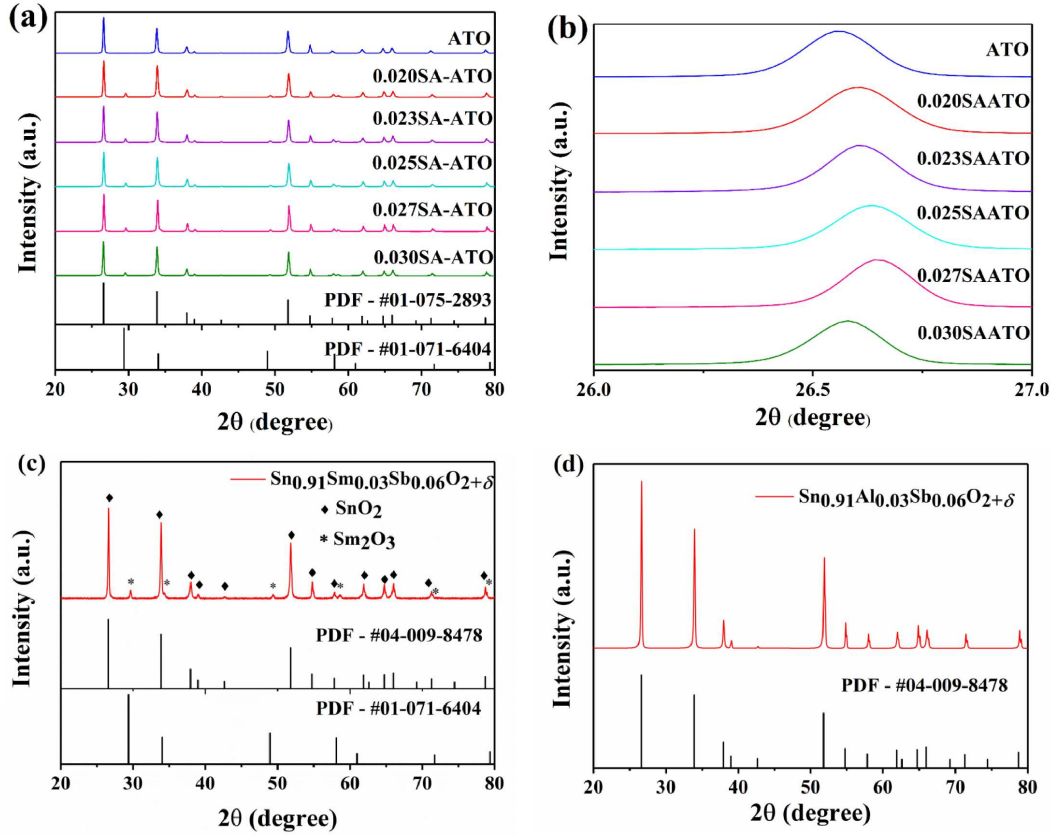


Figure 1. XRD patterns of sintered ceramics: a) ATO and zSA-ATO, b) enlarged 2θ for the corresponding ceramics, c) $\text{Sn}_{0.91}\text{Sm}_{0.03}\text{Sb}_{0.06}\text{O}_{2+\delta}$ and d) $\text{Sn}_{0.91}\text{Al}_{0.03}\text{Sb}_{0.06}\text{O}_{2+\delta}$

Table 1. Lattice parameters, measured densities D_m , lattice densities D_l , and relative densities D_r of sintered ceramics

Sample	Lattice parameters		D_m [g/cm ³]	D_l [g/cm ³]	D_r
	$a = b$ [nm]	c [nm]			
ATO	4.7369	3.1881	6.6839	6.9955	0.9554
0.020SA-ATO	4.7306	3.1811	6.4946	6.9982	0.9281
0.023SA-ATO	4.7305	3.1808	6.5065	6.9859	0.9314
0.025SA-ATO	4.7287	3.1772	6.4239	6.9905	0.9189
0.027SA-ATO	4.7262	3.1767	6.4073	6.9904	0.9166
0.030SA-ATO	4.7323	3.1791	6.3913	6.9713	0.9168

to form solid solution, but the significantly larger Sm-ion substituted into Sn^{4+} site and led to a large lattice distortion.

Figure 2 represents the cross-sectional SEM observation and element distribution mapping of the 0.030SA-ATO sample. Tightly connected particles with an average size less than $5\mu\text{m}$ can be recognised (Figs. 2a and 2b). According to the density measurement by the Archimedes method, the relative densities (D_r) of the ATO, 0.020SA-ATO, 0.023SA-ATO, 0.025SA-ATO, 0.027SA-ATO and 0.030SA-ATO ceramics were 95.5, 92.8, 93.1, 91.9, 91.7 and 91.7%TD, respectively. To investigate the composition distribution in the 0.030SA-ATO ceramics, EDS analysis was conducted. Figures 2c-2h show the elemental distribution mappings of Sn, Sb, O, Cu, Al and Sm, respectively. The element Al and Sb are uniformly distributed in ceramics. However, there is a significant distribution differ-

ence in elements Sn, Cu and Sm. Combined with the XRD results in Fig. 1, the Sm-rich regions should belong to the Sm_2O_3 phase. The Cu-rich regions should result from the sintering aid CuO. SEM images with the corresponding elemental distribution mappings of the 0.03Sm-ATO and 0.03Al-ATO ceramics are shown in Fig. 3. These results are consistent with Figs. 1c and 1d, indicating that there is a uniform distribution of elements and impurity phase in the 0.03Al-ATO, while the 0.03Sm-ATO ceramics has Sm-rich regions.

To investigate the valance state of Sb- and Sm-ions, XPS analyses of the sintered ceramics were conducted. The XPS full spectra of the 0.03Al-ATO and 0.030SA-ATO ceramics are shown in Fig. 4. The XPS spectra around the Sb $3d_{3/2}$ peak in the sintered 0.03Al-ATO and 0.030SA-ATO ceramics are shown in Figs. 5a and 5b, respectively. After being fitted using the Advantage program, the XPS peak of Sb $3d_{3/2}$ could be regarded

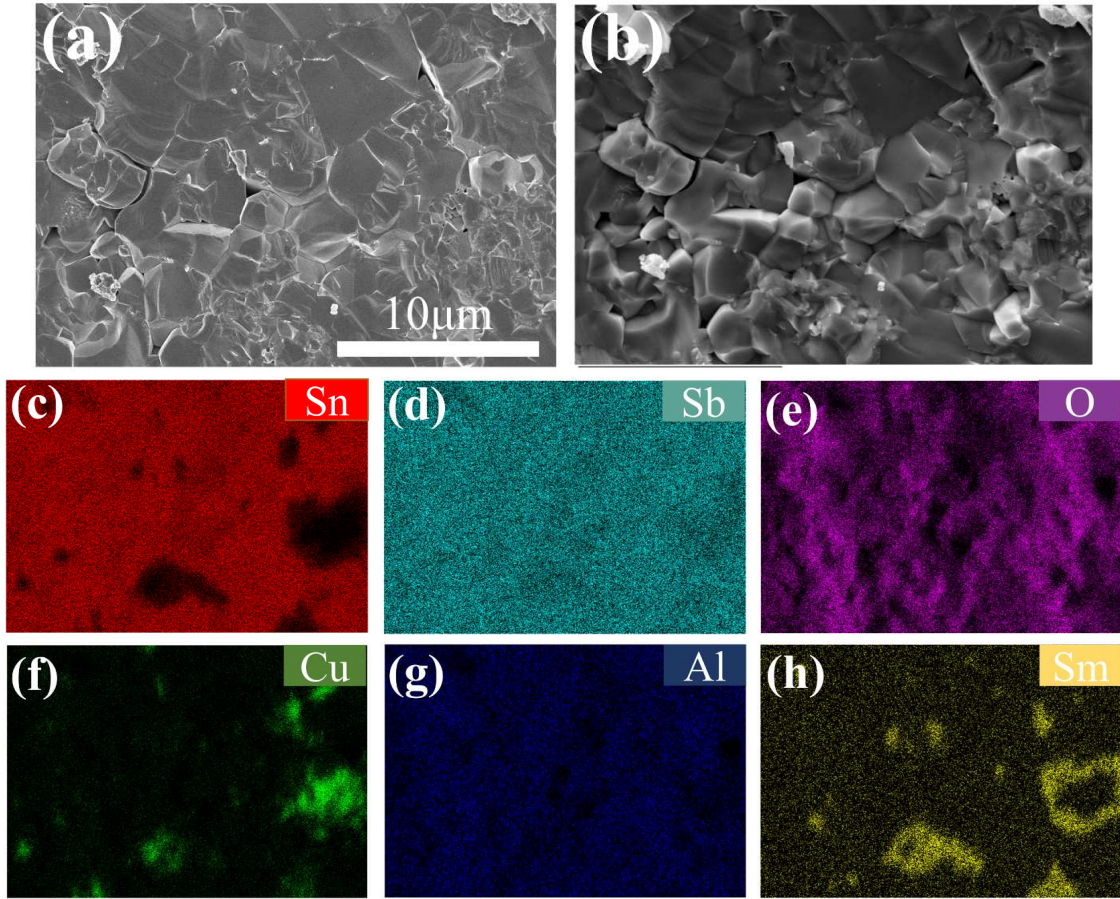


Figure 2. SEM and EDS analyses of 0.030SA-ATO ceramics: a) secondary electron image, b) backscattered electron image and c-h) element distribution mappings of Sn, Sb, O, Cu, Al and Sm, respectively

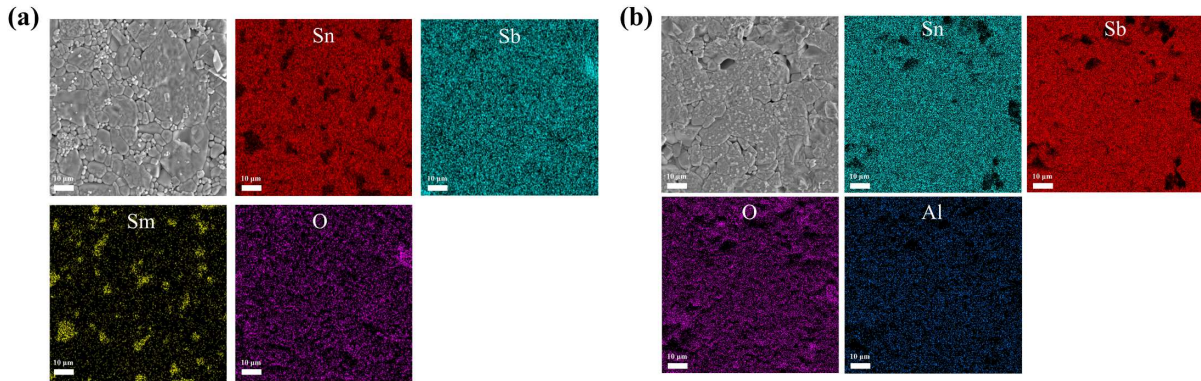


Figure 3. SEM images and related EDS element distribution mapping of prepared ceramics: a) $\text{Sn}_{0.91}\text{Sm}_{0.03}\text{Sb}_{0.06}\text{O}_{2+\delta}$ and b) $\text{Sn}_{0.91}\text{Al}_{0.03}\text{Sb}_{0.06}\text{O}_{2+\delta}$

as superimposed by two splitting peaks at 540.1 and 539.4 eV corresponding to Sb^{5+} and Sb^{3+} , respectively. To compare the relative content of two valence states of ions, the areas of fitted peaks were calculated. The content ratios of $[\text{Sb}^{5+}]/[\text{Sb}^{3+}]$ were 3.57 and 3.13 for the 0.03Al-ATO and 0.030SA-ATO ceramics, respectively. Figure 5c shows the XPS spectrum around Sm $3d_{5/2}$ peak of the 0.030SA-ATO ceramics. The spectrum could be superimposed by two splitting peaks at 1083.1 eV (Sm^{3+}) and 1078.4 eV (Sm^{2+}). The content ratio of $[\text{Sm}^{3+}]/[\text{Sm}^{2+}]$ was 2.44.

3.2. Electrical properties

The pure ATO ceramics has ρ_{25} of $8.3 \Omega\text{-cm}$ and B value of 328 K, which are in agreement with the previous reports [29–31]. This indicates that doping of Sb-ions can effectively make SnO_2 semiconducting and reduce the ceramics resistivity. During the calcination and sintering process, the Sb^{3+} ions from the raw material Sb_2O_3 could be oxidized to Sb^{5+} ions as shown in the XPS analysis in Fig. 5, and the $[\text{Sb}^{5+}]/[\text{Sb}^{3+}]$ ratios are much higher than 1, implying that the content of Sb-ions

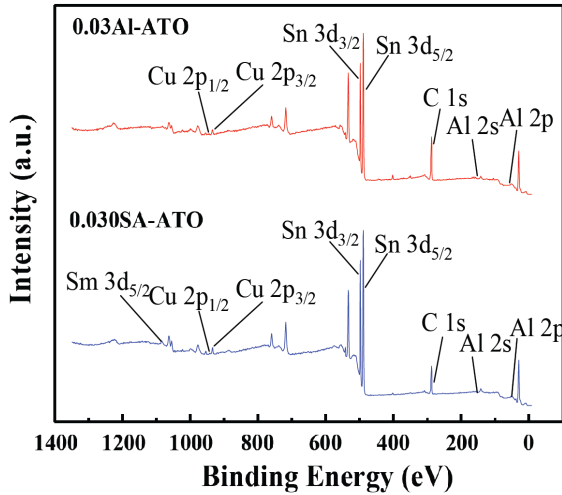
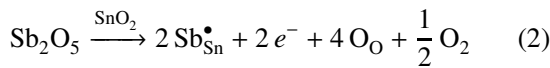


Figure 4. XPS spectra of sintered 0.03Al-ATO and 0.03SA-ATO ceramics before ageing

in ATO mainly acted as donors and resulted in the formation of electron charge carriers as presented in Eq. 2:



The electrons were weakly bounded around the Sb^{5+} donor level. According to the report by White *et al.* [32],

the activation energy for the Sb^{5+} donor ionization or the weakly bounded electrons to jump from donor level to conduction band is very small (27.1 meV). So the weakly bounded electrons can be easily thermally activated to the conduction band in SnO_2 based semiconductor, producing electrical conductivity of ceramics. As analysed in Fig. 5, the content ratio of $[\text{Sb}^{5+}]/[\text{Sb}^{3+}]$ is higher than 3, i.e. the content of Sb^{5+} ions is much higher than the one of Sb^{3+} ions, so the ATO ceramics have *n*-type semiconductor characteristics. The high electron concentration enhances the electrical conductivity. So the band conduction mode plays an important role in electrical conductivity of the ATO ceramics.

The electrical properties of *z*SA-ATO ceramics (Fig. 6) display typical NTC effect. $B_{25/85}$ and ρ_{25} show obvious change with the change of Al content, i.e. ρ_{25} values were 0.25, 0.72, 2.05, 24.06 and 49.93 k Ω -cm and $B_{25/85}$ values were 2204, 2687, 2937, 3407 and 4022 K for *z* equal to 0.020, 0.023, 0.025, 0.027 and 0.030, respectively. The Al-doped ATO (*x*Al-ATO) and Sm-doped ATO ceramics (*y*Sm-ATO) have the similar change trend as shown in Fig. 7. The change of electrical properties for the Al-ATO should result from the solid solution of Al-ions in ATO lattice. Since Al^{3+} has lower valence than Sn^{4+} ion, it acted as acceptor in ATO and induced the formation of electronic holes as presented in Eq. 3:

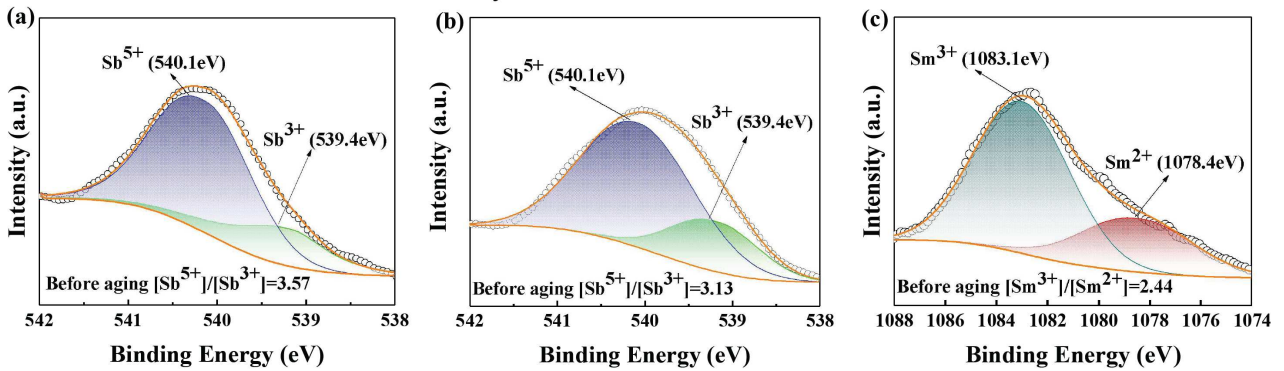


Figure 5. Selected region of XPS spectra of: a) Sb $3d_{3/2}$ for 0.03Al-ATO, b) Sb $3d_{3/2}$ for 0.030SA-ATO and d) Sm $3d_{5/2}$ for 0.030SA-ATO samples

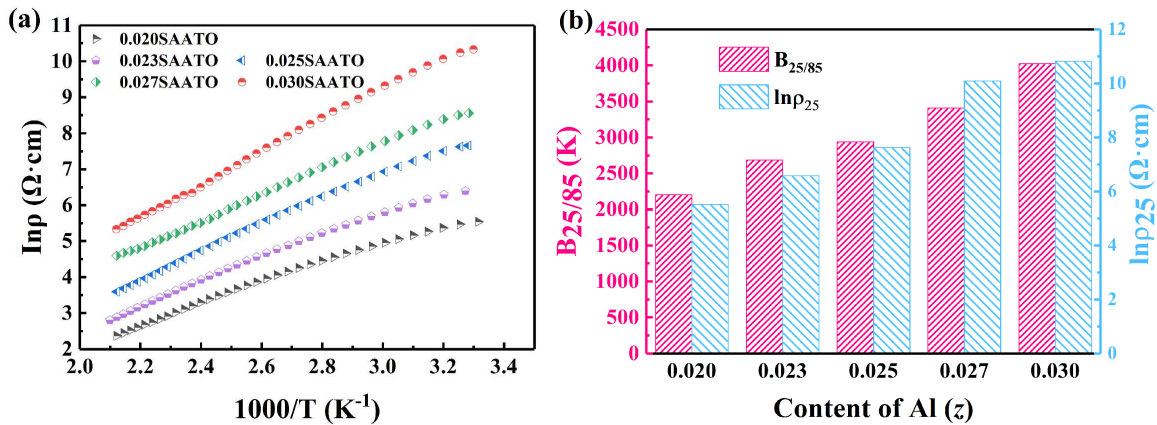


Figure 6. Electrical properties of *z*SA-ATO with various Al-ion contents: a) temperature dependence of resistivity in $\ln\rho-1000/T$ plot and b) Al-content dependence of $B_{25/85}$ and ρ_{25}

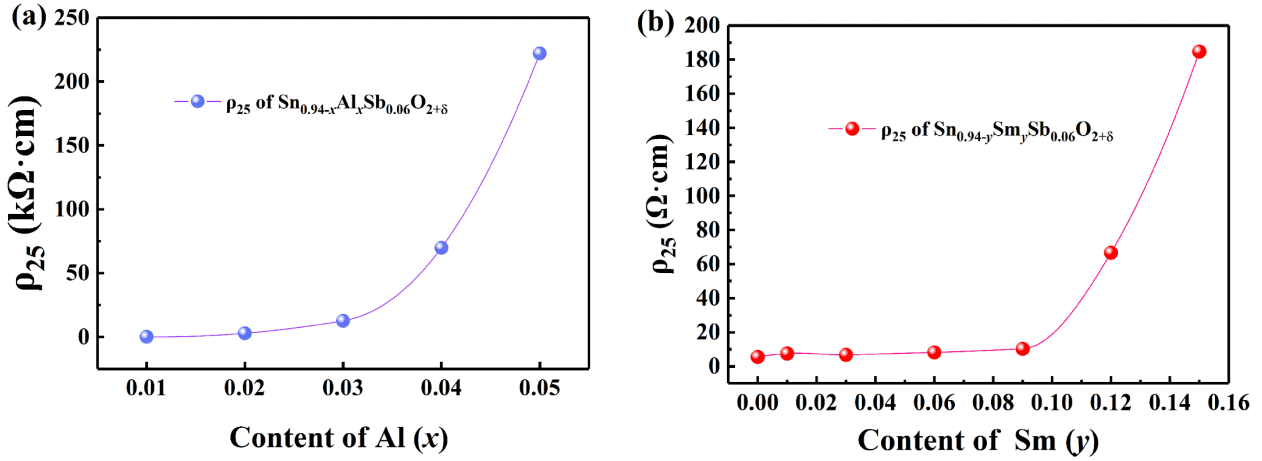


Figure 7. Room temperature resistivity (ρ_{25}) of: a) $\text{Sn}_{0.94-x}\text{Al}_x\text{Sb}_{0.06}\text{O}_{2+\delta}$ and b) $\text{Sn}_{0.94-y}\text{Sm}_y\text{Sb}_{0.06}\text{O}_{2+\delta}$

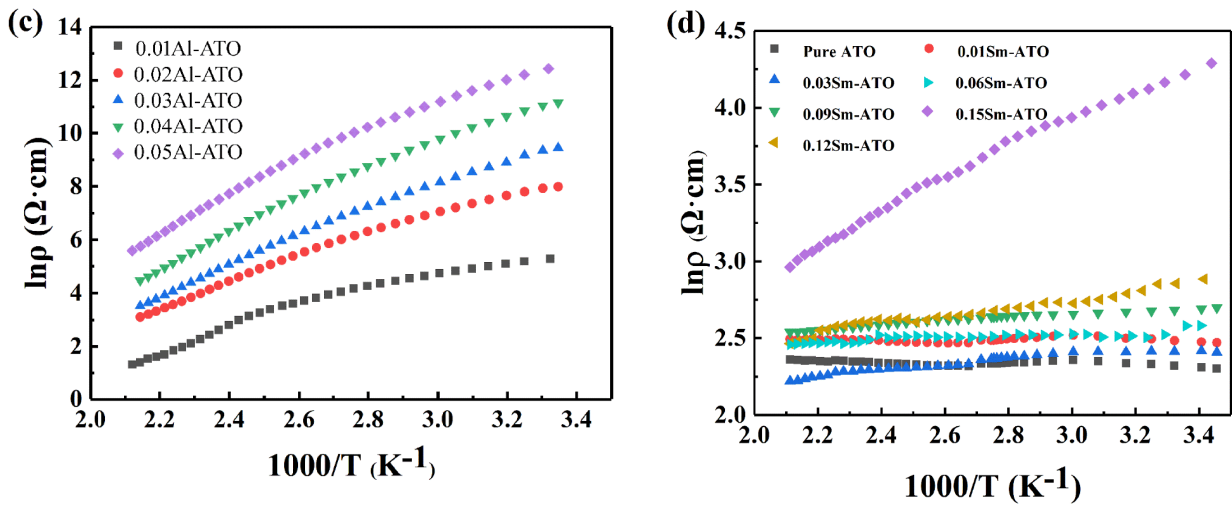
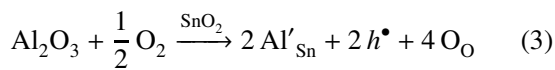


Figure 8. $\ln\rho - 1000/T$ plots of: a) $\text{Sn}_{0.94-x}\text{Al}_x\text{Sb}_{0.06}\text{O}_{2+\delta}$ and b) $\text{Sn}_{0.94-y}\text{Sm}_y\text{Sb}_{0.06}\text{O}_{2+\delta}$ ceramics



The Al-doping increased the concentration of holes in ATO lattice. The combination of charge holes induced by Al^{3+} ions and electrons induced by Sb^{5+} ions led to the decrease in the concentration of effective charge carriers and the increase of resistivity. In addition, the $\ln\rho - 1000/T$ plots of the sintered $\text{Sn}_{0.94-x}\text{Al}_x\text{Sb}_{0.06}\text{O}_{2+\delta}$ and $\text{Sn}_{0.94-y}\text{Sm}_y\text{Sb}_{0.06}\text{O}_{2+\delta}$ ceramics are presented in Fig. 8.

To further reveal the electrical properties of the prepared ceramics, EIS analysis was conducted. The Nyquist plots of the 0.030SA-ATO ceramics measured at various temperatures are shown in Fig. 9a. An equivalent circuit (inset in Fig. 9a) was used to fit the EIS data. R_g and R_{gb} represent resistances from grain effect and grain boundary effect, respectively. CPE_1 and CPE_2 are constant phase elements from grain effect and grain boundary effect, respectively, for the existence of point defects and non-uniform structural characteristics inside the material. Refined by Zview program, the resistances and capacitances for the grain effect and

grain boundary effect were calculated. The fitted results are presented in Table 2. The good fitting results indicate that the total resistance of each prepared ceramics comes from both grain effect and grain boundary effect. Plots of $\ln R_g$, $\ln R_{gb}$ and $\ln(R_g + R_{gb})$ versus $1000/T$ are shown in Fig. 9b. The fitted results reveal that R_g , R_{gb} and $R_g + R_{gb}$ have similar activation energies of conduction (E_a), i.e. 0.256, 0.255 and 0.257 eV, respectively. At each test temperature, the grain boundary resistance is much higher than the grain resistance, indicating that the contribution of grain boundaries to ceramics resistance is higher than the grains. As shown in Fig. 1, the existence of the secondary phase, such as Sm_2O_3 with poor electronic conductivity in the zSA-ATO ceramics resulted in high resistivity of grain boundary effect.

As shown in Figs. 7 and 9, the introduction of Sm/Al significantly increased ρ_{25} and $B_{25/85}$ of the ATO-based thermistors and has the same contribution from grain effect and grain boundary one. The activation energies of conduction (for the 0.030SA-ATO ceramics, activation energies for R_g , R_{gb} and $R_g + R_{gb}$ were 0.256, 0.255 and 0.257 eV, respectively) are much higher than that of the activation energy for Sb^{5+} ionization (27.1 meV).

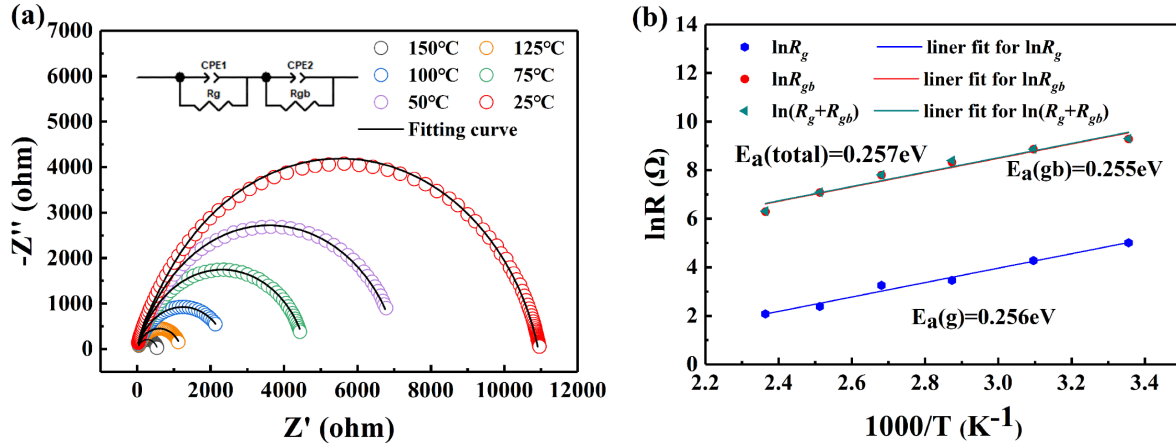


Figure 9. Analysis of AC impedance of 0.030SA-ATO at various temperatures: a) electrochemical impedance spectroscopy (point data) and fitted curves by the inset equivalent circuit and b) temperature dependence of R_g , R_{gb} and $R_g + R_{gb}$

Table 2. Fitting results of impedance spectra of 0.030SA-ATO at various temperatures

T [°C]	Grain fitting results		Grain boundary fitting results	
	Resistance [Ω]	Capacitance [F]	Resistance [Ω]	Capacitance [F]
25	149.64	2.89×10^{-9}	10778.45	1.48×10^{-8}
50	72.31	2.21×10^{-9}	7044.08	1.60×10^{-8}
75	35.75	1.98×10^{-9}	4406.78	1.78×10^{-8}
100	28.54	8.77×10^{-9}	2431.53	2.08×10^{-8}
125	11.23	6.78×10^{-10}	1204.37	3.56×10^{-8}
150	8.90	7.66×10^{-13}	534.88	2.37×10^{-8}

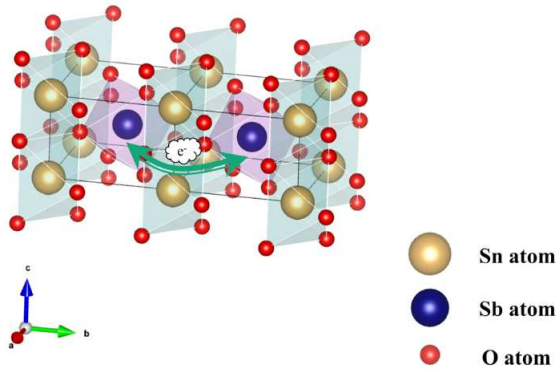


Figure 10. Illustration of hopping process in Sb-doped SnO_2

So the band conduction mode could not contribute to the high E_a , and there should be other possible conduction modes in the zSA-ATO ceramics.

As in most of the NTC thermistors, polaron hopping is one of the important conductive modes for the existence of valence-variable cations. The polaron hopping may take place between cations in adjacent oxygen octahedra, under thermal activation or external electric field. This is so-called polaron hopping mode. As discussed in XPS analysis in Fig. 5, the Sb- and Sm-cations have variable valences. Thus, the polaron hopping should be one of the conduction modes in the prepared ATO-based ceramics and described by following equations: $\text{Sb}^{3+} + \text{Sb}^{5+} \leftrightarrow \text{Sb}^{5+} + \text{Sb}^{3+}$ and $\text{Sm}^{3+} + \text{Sm}^{2+} \leftrightarrow \text{Sm}^{2+} + \text{Sm}^{3+}$. However, the latter is difficult to carry out because of the large hopping activation en-

ergy of Sm-cations [33]. Figure 10 illustrates the hopping process. For the hopping process, it is necessary for the conductive electrons to get rid of the binding of lower-valence cations, simultaneously, the electron must overcome the lattice barrier of oxygen octahedral. So the hopping process requires a large energy, resulting in larger conductive activation energy.

On the other hand, for the grain boundary conduction, charge carriers must overcome the grain boundary barriers to undergo migration. So the conductive activation energy of grain boundary effect is always high. Especially the existence of impurities at grain boundaries can further increase the interfacial barrier, and results in large E_a . These conductive modes should also be the main factors for electrical conduction, and also make great contribution to $B_{25/85}$. Higher temperatures easily excite electrons to overcome lattice barriers and grain boundary barriers, resulting in higher conductivity and the NTC effect with higher E_a .

3.3. Ageing stability

Figure 11 illustrates the ageing characteristics of the xAl-ATO and zSA-ATO ceramics. It can be seen from Fig. 11a that after 500 h ageing treatment, the resistance shifts of the xAl-ATO without Sm-ion are large. The largest resistance drift rate ($\Delta R/R$) is -75% . Figure 11b reveals that the introduction of Sm can effectively improve ageing stability of the Al-ATO. The resistance shift rate of the zSA-ATO can be maintained below -3% .

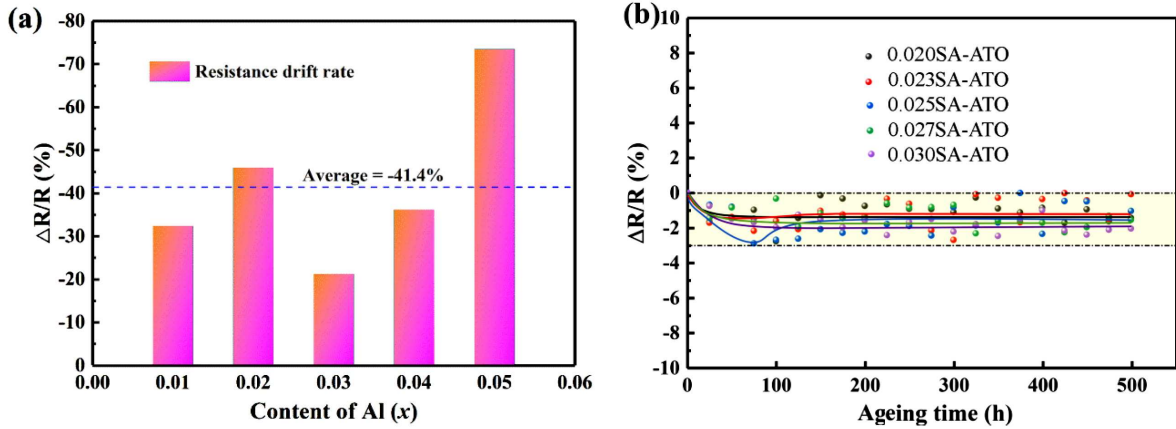


Figure 11. Ageing induced resistance shift of ceramics: a) x Al-ATO after 500 h and b) z SA-ATO during ageing 500 h

Figures 12 and 13 illustrate XPS analyses of the 0.03Al-ATO and 0.030SA-ATO ceramics after ageing at 150 °C for 500 h. These data were received from the same samples as that shown in Figs. 4 and 5 (before ageing treatment). Figure 12 shows the XPS full spectra of the 0.03Al-ATO and 0.030SA-ATO ceramics after ageing. Figures 13a and 13b are Sb $3d_{3/2}$ XPS spec-

tra of the 0.03Al-ATO and 0.030SA-ATO ceramics after ageing, respectively. The fitted peaks corresponding to Sb^{5+} and Sb^{3+} are located at 540.1 and 539.5 eV or 539.6 eV, respectively. Compared with the data shown in Fig. 5a, the content ratios of $[Sb^{5+}]/[Sb^{3+}]$ in the 0.03Al-ATO ceramics changed from 3.57 to 1.32, indicating that the relative content of Sb^{3+} increased during ageing process. Figs. 5b and 13b represent the Sb $3d_{3/2}$ XPS spectrum of the 0.030SA-ATO ceramics before and after ageing, respectively. The effect of ageing on the valance state of Sb element is similar to that of the 0.03Al-ATO ceramics, the $[Sb^{5+}]/[Sb^{3+}]$ ratio was reduced from 3.13 to 1.16. Figure 13c displays Sm $3d_{5/2}$ XPS spectrum of the 0.030SA-ATO ceramics after ageing, and the peak position corresponding to Sm^{3+} and Sm^{2+} are at 1083.1 and 1078.4 eV, respectively. When comparing the Sm $3d_{5/2}$ XPS spectra of the 0.030SA-ATO presented in Figs. 5c and 13c, the content ratio of $[Sm^{3+}]/[Sm^{2+}]$ decreased from 2.44 to 1.25.

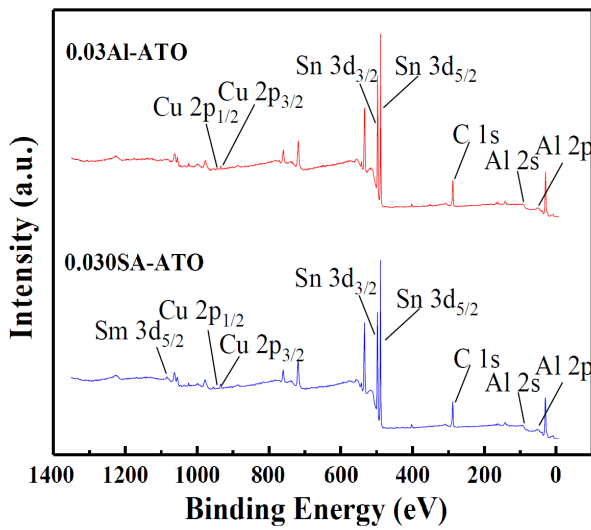


Figure 12. XPS spectra of sintered 0.03Al-ATO and 0.03SA-ATO ceramics after ageing

The decrease of the sample resistance should result from the increase of the concentration of charge carriers. As mentioned in section 3.2, electron is the predominant carrier in the ATO system. During ageing process, the moist in air would be adsorbed on the surface of ceramics and then react with the holes that come from the acceptor doping (Al^{3+} or Sb^{3+}) as shown in Eqs. 4 and 5. The combination of electrons and holes in the ceramics

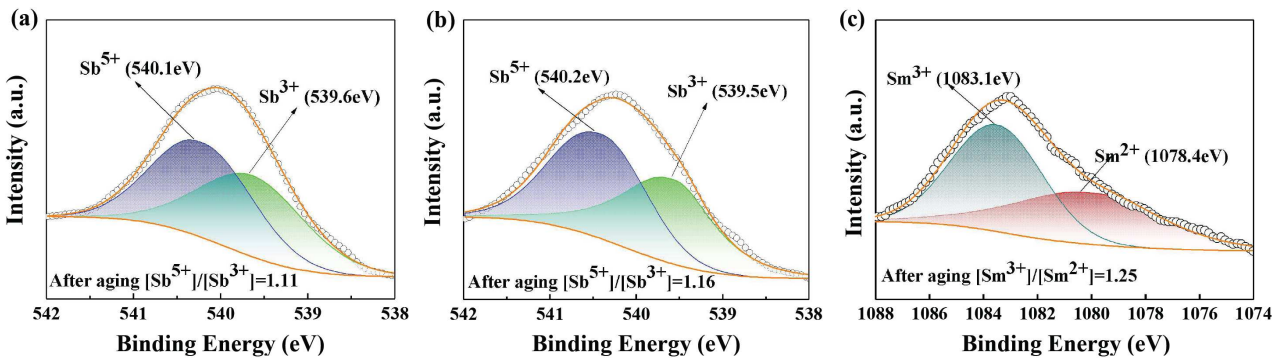
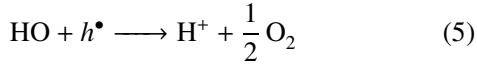


Figure 13. Selected region of XPS spectra of: a) Sb $3d_{3/2}$ for 0.03AATO, b) Sb $3d_{3/2}$ for 0.030SAATO and c) Sm $3d_{5/2}$ for 0.030SAATO

was suppressed, and the decrease in the amount of holes led to more charge carrier electrons. Thus, the resistance of ceramics decreased.



During the ageing process, the concentration of charge carrier electrons from the Sb^{5+} donors increased, and enhanced the conductivity of material. Based on the analysis of XPS, Sb and Sm have two valences. In the $x\text{Al}$ -ATO and $z\text{SA}$ -ATO ceramics, the contents of Sb-ions changed obviously, and the $[\text{Sb}^{5+}]/[\text{Sb}^{3+}]$ ratios changed from 3.57 to 1.32, and from 3.13 to 1.16, respectively. This process simultaneously consumed a certain amount of excess electrons. Figure 14 illustrates the effect of Sm_2O_3 on the ageing process in the $z\text{SA}$ -ATO ceramics. There are a few Sm_2O_3 particles or traces among the doped ATO crystals. Since during the ageing process Sm^{3+} could be reduced to Sm^{2+} , the $[\text{Sm}^{3+}]/[\text{Sm}^{2+}]$ ratio decreased from 2.44 to 1.25 as discussed in the XPS analysis. This process further reduced electron concentration so the conductivity is relatively stable with the introduction of Sm-ions.

Based on the polaron hopping mode, the temperature dependent conductivity (σ) is commonly described by the Nernst-Einstein formula [18]:

$$\sigma = \frac{N \cdot c \cdot (1 - c) \cdot N_{oct} \cdot e^2 \cdot d^2 \cdot \nu_0}{k \cdot T} \cdot \exp\left(-\frac{T_0}{T}\right) \quad (6)$$

where k is the Boltzmann constant, T is actual temperature, e is electron charge, d is hopping distance, ν_0 is hopping frequency and T_0 is defined as the characteristic temperature. N_{oct} is the concentration of octahedral sites as it was first applied to describe the conductive process of spinel type compounds, and it can be seen as the concentration of the sites that can undergo hopping in compounds with other crystal. The factor $Nc(1 - c)$ denotes the probability that transition ions pairs occupy the adjacent octahedrons, where N is the concentration of sites per formula unit which are available to the charge carriers, and c can be defined

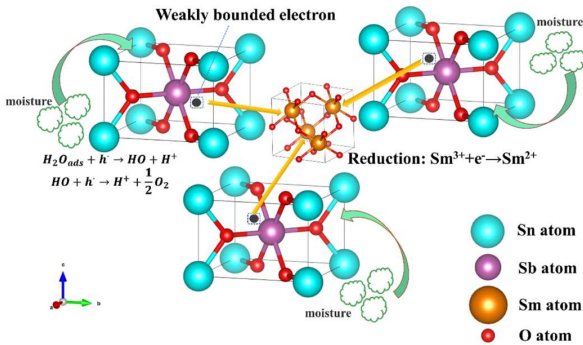


Figure 14. XPS spectra of sintered 0.03Al-ATO and 0.03SA-ATO ceramics after ageing

as $[\text{Sb}^{5+}]/([\text{Sb}^{5+}] + [\text{Sb}^{3+}])$. According to Eq. 6, when the ratio of $[\text{Sb}^{5+}]/([\text{Sb}^{5+}] + [\text{Sb}^{3+}])$ changes to 0.5, i.e. $[\text{Sb}^{5+}]/[\text{Sb}^{3+}]$ ratio changes to 1, the conductivity increases. From Figs. 5 and 13, the ratios of $[\text{Sb}^{5+}]/[\text{Sb}^{3+}]$ changed from 3.57 to 1.11 in the 0.03Al-ATO ceramics and from 3.13 to 1.16 in the 0.030SA-ATO ceramics. Thus, the conductivity originating from hopping mechanism would also be enhanced.

IV. Conclusions

A series of $\text{Sn}_{0.94-x-y}\text{Al}_x\text{Sm}_y\text{Sb}_{0.06}\text{O}_{2+\delta}$ ceramics were fabricated by a solid-state reaction method and sintering at 1350 °C for 2 h. The Al-doped $\text{Sn}_{0.94}\text{Sb}_{0.06}\text{O}_2$ (ATO) ceramics have single phase tetragonal structure, while the Sm/Al co-doped ATO ceramics have structure with main tetragonal phase and an impurity Sm-rich phase. All the prepared ceramics show typical NTC characteristics. The Al-doped ATO ceramics without Sm-ion have adjustable room temperature resistivity (ρ_{25}) and high material constant ($B_{25/85}$) with changing Al-ion content, but the related ageing stability is poor. The Sm/Al co-doped ATO ceramics have wide adjustable $B_{25/85}$ (ranging from 2204 to 4022 K) and ρ_{25} (ranging from 0.25 to 49.93 kΩ·cm), and the ageing stability is obviously improved. The moisture adsorption and the holes consumption in crystal accompanied by the increase of electron content are the mechanisms for the ageing-induced reduction of resistivity. Band conduction, hopping conduction and overcoming boundary barriers of electron migration are proposed for the simultaneous conduction modes in the prepared NTC ceramics.

Acknowledgements: This work is supported by the research funds from the Development Funds of Hunan Wedid Materials Technology Co., Ltd., China (No. 738010241), and the Foundation of the Department of Science and Technology of Guizhou province, China (No. CG[2021]110), and the Foundation of the Department of Education of Guizhou province, China (No. QJJ[2022]003).

References

1. A. Feteira, “Negative temperature coefficient resistance (NTCR) ceramic thermistors: an industrial perspective”, *J. Am. Ceram. Soc.*, **92** (2009) 967–983.
2. K. Li, Z. Li, Y. Wen, Y. Zhan, H. Zhang, “Mn/La co-doped WO_3 ($\text{Mn}_x\text{La}_{0.03}\text{WO}_{3+\delta}$, $x \leq 0.1$) ceramics for NTC thermistors”, *J. Mater. Sci. Mater. Electron.*, **35** (2024) 725.
3. J. Liu, Q. Guo, W. Liang, X. Feng, H. Wang, “On the NTC behaviors in explosion limits of C1 to C3 n-alkane/air mixtures”, *Energy*, **294** (2024) 130785.
4. Y. Chen, G. Yang, J. Wang, Y. Lu, H. Shen, X. Zhang, S. Liang, “A novel linear temperature thermistor in the $x\text{Al}_2\text{O}_3$ -(1-x) CdSnO_3 system”, *Ceram. Int.*, **50** (2024) 12607–12613.
5. M. Hosseini, B. Yasaei, “Effect of grain size and microstructures on resistivity of Mn-Co-Ni thermistor”, *Ce-*

- ram. Int., **24** (1998) 543–545.
6. J. Wang, J. Zhang, “Structural and electrical properties of $\text{NiMg}_x\text{Mn}_{2-x}\text{O}_4$ NTC thermistors prepared by using sol-gel derived powders”, *Mater. Sci. Eng. B*, **176** (2011) 616–619.
 7. L. Chen, W. Kong, J. Yao, B. Gao, Q. Zhang, H. Bu, A. Chang, C. Jiang, “Effect of sintering temperature on microstructure and electrical properties of $\text{Mn}_{1.2}\text{Co}_{1.5}\text{Ni}_{0.3}\text{O}_4$ ceramic materials using nanoparticles by reverse microemulsion method”, *J. Mater. Sci. Mater. Electron.*, **27** (2016) 1713–1718.
 8. Y. Zeng, Z. Li, C. Gao, G. Jiang, H. Zhang, “Electrical conductivity and temperature sensitivity of Cu/Mo co-modified YFeO_3 ceramics”, *Process. Appl. Ceram.*, **15** (2021) 195–201.
 9. Y. Zeng, Z. Li, J. Shao, X. Wang, W. Hao, H. Zhang, “Electrical properties of perovskite YFeO_3 based ceramics modified by Cu/Nb ions as negative temperature coefficient thermistors”, *J. Mater. Sci. Mater. Electron.*, **30** (2019) 14528–14537.
 10. C. Ma, H. Gao, “TEM and electrical properties characterizations of $\text{Co}_{0.98}\text{Mn}_{2.02}\text{O}_4$ NTC ceramic”, *J. Alloys Compd.*, **749** (2018) 853–858.
 11. F. Guan, Z. Dang, X. Chen, S. Huang, J. Wang, X. Cheng, Y. Wu, “Novel electrical properties of Mn-doped LaCrO_3 ceramics as NTC thermistors”, *J. Alloys Compd.*, **871** (2021) 159269.
 12. S. Zhang, H. Zhang, S. Leng, Y. Wen, H. Wang, Z. Li, “Electrical properties and aging characteristic of Sb/Ga co-doped single-cation oxide SnO_2 ”, *J. Mater. Sci. Mater. Electron.*, **33** (2022) 23821–23833.
 13. G. Jiang, Z. Li, C. You, W. Hao, Z. Ma, H. Zhang, “Temperature sensitivity and electrical stability of Sb/Mn co-doped SnO_2 ceramics”, *J. Mater. Sci. Mater. Electron.*, **32** (2021) 16945–16955.
 14. X. Xu, M. Yin, N. Li, W. Wang, B. Sun, M. Liu, D. Zhang, Z. Li, C. Wang, “Vanadium-doped tin oxide porous nanofibers: Enhanced responsivity for hydrogen detection”, *Talanta*, **167** (2017) 638–644.
 15. T.S. Zhang, L.B. Kong, X.C. Song, Z.H. Du, W.Q. Xu, S. Li, “Densification behaviour and sintering mechanisms of Cu- or Co-doped SnO_2 : A comparative study”, *Acta Mater.*, **62** (2014) 81–88.
 16. X. Wang, Z. Li, P. Wang, W. Yan, H. Zhang, “Electrical properties of Nb/Al doped CuO-based ceramics for NTC thermistors”, *Process. Appl. Ceram.*, **14** (2020) 47–55.
 17. Z. Yang, H. Zhang, Z. He, B. Li, Z. Li, “Influence of B^{3+} - and Na^+ -ions on electrical property and temperature sensitivity of NiO-based ceramics”, *J. Mater. Sci. Mater. Electron.*, **30** (2019) 3088–3097.
 18. L. Huang, Z. Li, K. Li, Y. Zhang, H. Zhang, S. Leng, “Electrical conductivity and electrical stability of Bi/Mg modified NiO ceramics for NTC thermistors”, *Process. Appl. Ceram.*, **17** (2023) 172–180.
 19. P. Li, H. Zhang, C. Gao, G. Jiang, Z. Li, “Electrical property of Al/La/Cu modified ZnO-based negative temperature coefficient (NTC) ceramics with high ageing stability”, *J. Mater. Sci. Mater. Electron.*, **30** (2019) 19598–19608.
 20. B. Yang, H. Zhang, J. Guo, Y. Liu, Z. Li, “Electrical properties and thermal sensitivity of Ti/Y modified CuO-based ceramic thermistors”, *Front. Mater. Sci.*, **10** (2016) 413–421.
 21. J. Zhang, H. Zhang, B. Yang, Y. Zhang, Z. Li, “Temperature sensitivity of Fe-substituted SnO_2 -based ceramics as negative temperature coefficient thermistors”, *J. Mater. Sci. Mater. Electron.*, **27** (2016) 4935–4942.
 22. S. Zheng, Y. Li, J. Hao, H. Fang, Y. Yuan, H-S Tsai, Q. Sun, P. Wan, X. Zhang, Y. Wang, “Hierarchical assembly of graphene-bridged SnO_2 -rGO/ SnS_2 heterostructure with interfacial charge transfer highway for high-performance NO_2 detection”, *Appl. Surf. Sci.*, **568** (2021) 150926.
 23. Y. Song, X. Wang, X. Zhang, X. Qi, Z. Liu, L. Zhang, Y. Zhang, Y. Wang, Y. Sui, B. Song, “Colossal dielectric permittivity in (Al + Nb) co-doped rutile SnO_2 ceramics with low loss at room temperature”, *Appl. Phys. Lett.*, **109** (2016) 142903.
 24. D. Liu, W. Wang, K. Cheng, Q. Xie, Y. Zhou, H. Zhao, “High voltage gradient and low leakage current SnO_2 varistor ceramics doped with Y_2O_3 and Nb_2O_5 ”, *Mater. Chem. Phys.*, **242** (2020) 122526.
 25. I. Saadeddin, H.S. Hilal, B. Pecquenard, J. Marcus, A. Mansouri, C. Labrugere, M.A. Subramanian, G. Campet, “Simultaneous doping of Zn and Sb in SnO_2 ceramics: Enhancement of electrical conductivity”, *Solid State Sci.*, **8** (2006) 7–13.
 26. U. Zum Felde, M. Haase, H. Weller, “Electrochromism of highly doped nanocrystalline SnO_2 :Sb”, *J. Phys. Chem. B*, **104** (2000) 9388–9395.
 27. J.T.S. Irvine, D.C. Sinclair, A.R. West, “Electroceramics: characterization by impedance spectroscopy”, *Adv. Mater.*, **2** (1990) 132–138.
 28. R.D. Shannon, “Revised effective ionic radii and systematic studies of interatomic distances in halides and chalcogenides”, *Acta Cryst. A*, **32** (1976) 751–767.
 29. T. Boucherka, M. Touati, A. Berbadj, N. Brihi, “ Al^{3+} doping induced changes of structural, morphology, photoluminescence, optical and electrical properties of SnO_2 thin films as alternative TCO for optoelectronic applications”, *Ceram. Int.*, **49** (2023) 5728–5737.
 30. Y. Zhang, Y. Wu, H. Zhang, W. Chen, G. Wang, Z. Li, “Characterization of negative temperature coefficient of resistivity in $(\text{Sn}_{1-x}\text{Ti}_x)_{0.95}\text{Sb}_{0.05}\text{O}_2$ ($x \leq 0.1$) ceramics”, *J. Mater. Sci. Mater. Electron.*, **25** (2014) 5552–5559.
 31. P. Ouyang, H. Zhang, Y. Zhang, J. Wang, Z. Li, “Zr-substituted SnO_2 -based NTC thermistors with wide application temperature range and high property stability”, *J. Mater. Sci. Mater. Electron.*, **26** (2015) 6163–6169.
 32. M.E. White, O. Bierwagen, M.Y. Tsai, J.S. Speck, “Electron transport properties of antimony doped SnO_2 single crystalline thin films grown by plasma-assisted molecular beam epitaxy”, *J. Appl. Phys.*, **106** (2009) 093704.
 33. J. Mucha, H. Misiorek, A.V. Golubkov, L.S. Parfenieva, I.A. Smirnov, “Thermal conductivity of Sm_3S_4 system with mixed valence Sm ions”, *Int. J. Thermophys.*, **24** (2003) 859–865.